

# Modeling Fault Recovery and Transient Stability of Grid-Forming Converters Equipped With Current Reference Limitation

Ali Arjomandi-Nezhad, *Student Member, IEEE*, Yifei Guo, *Member, IEEE*, Bikash C. Pal, *Fellow, IEEE*, Guangya Yang, *Senior Member, IEEE*.

**Abstract**—When grid-forming (GFM) inverter-based resources (IBRs) face severe grid disturbances (e.g., short-circuit faults), the current limitation mechanism may be triggered. Consequently, the GFM IBRs enter the current-saturation mode, inducing nonlinear dynamical behaviors and posing great challenges to the post-disturbance transient angle stability. This paper presents a systematic study to reveal the fault recovery behaviors of a GFM IBR and identify the risk of instability. A closed-form expression for the necessary condition that a GFM IBR returns from the current-saturation mode to the normal operation mode is presented. Based on these analyses, it is inferred that the angle of the magnitude-saturated current significantly affects the post-fault recovery and transient stability; with different angle selection, the system may follow multiple post-fault trajectories depending on those conditions: 1) Convergence to a normal stable equilibrium point (SEP), 2) convergence to a saturated stable equilibrium point (satSEP), or 3) divergence (instability). In this paper, the circumstances under which a GFM IBR cannot escape from the current-saturation mode are thoroughly investigated. The theoretical analyses are verified by dynamic simulations.

**Index Terms**—Current limitation, current saturation, grid-forming (GFM) converters, post-fault recovery, transient stability, virtual synchronous generator (VSG).

## I. INTRODUCTION

**R**ETIREMENT of conventional synchronous generator-based power plants in favor of inverter-based resources (IBRs) made it necessary to implement grid-forming (GFM) control to provide various services, e.g. frequency and voltage support [1]–[4]. Nevertheless, GFM IBRs equipped with the current limitation/saturation exhibit complicated nonlinear dynamics during and after large disturbances [5], affecting the

system stability. Therefore, it is vital to study and model their responses to large disturbances.

The ability of GFM IBRs to retain synchronism with the grid after being subjected to a large disturbance is defined as their transient stability [6]. Since a GFM IBR usually synchronizes itself to the grid through the active power controller (APC), its transient stability can be redefined as the stability of the angle and frequency of APC around the stable equilibrium point (SEP) [4], [7]. Several papers studied the transient stability of GFM IBRs around the SEP by adopting Lyapunov-based methods [8], [9], Krylov–Bogoliubov–Mitropolsky asymptotic method [10], quantitative parameters constraining [11], [12], and damping energy visualization and geometry approximation [13]. However, these papers neglected the impact of current saturation on the dynamics of GFM IBRs. Unlike SGs, GFM IBRs usually have rather limited overcurrent capability, which is between 1.1 and 1.4 per unit (p.u.) if the GFM IBRs are not oversized [14], and therefore very easy to hit during disturbances. It has been demonstrated in the literature that the current saturation adversely affects the transient stability [4], [5].

Relatively fewer papers considered the current limitation in transient stability analysis. Generally, there are two categories of current limitation methods [15]: virtual impedance (VI) and current reference saturation (CRS). The former reduces the GFM voltage reference, whereas the latter directly limits the current reference generated by the voltage controller. References [16]–[19] studied transient stability of the VI-based current-limited GFM IBRs. Although the VI-based methods preserve the voltage source behavior, they may fail to limit the current within the first few milliseconds [15], [20]. In contrast, CRS-based methods limit the current promptly. Activation of CRS causes GFM IBRs to act as a current source while still being synchronized to the grid through the active power controller.

CRS can be implemented in several ways. Circular CRS, which generates a reference with maximum magnitude and the angle of unsaturated current, is usually used in cascade with a virtual admittance voltage controller [21]. Circular CRS is not usually cascaded with other types of voltage controllers. Other common types of CRS methods are d-axis priority CRS [23], q-axis priority CRS [24], and constant angle CRS

This work was supported in part by the European Union’s Horizon 2020 Research and Innovation Programme under the Marie Skłodowska-Curie Grant 956433 (InnoCyPES Project), in part by the Resilient Operation of Sustainable Energy Systems (ROSES) U.K.-China (EPSRC-NSFC) Programme on Sustainable Energy Supply under Grants EP/T021713/1 and NSFC-52061635102, and in part by the Royal Society under Grant RG\R2\232398. For the purpose of open access, the authors have applied a Creative Commons Attribution (CC BY) license to any Accepted Manuscript version arising.

A. Arjomandi-Nezhad (corresponding author) and B. C. Pal are with the Department of Electrical and Electronics Engineering at Imperial College London, London SW7 2AZ, United Kingdom (e-mails: a.arjomandi.nezhad21@imperial.ac.uk; b.pal@imperial.ac.uk).

Y. Guo is with the Key Laboratory of Power System Intelligent Dispatch and Control of Ministry of Education, Shandong University, Jinan 250061 (e-mail: yifei.guo@sdu.edu.cn).

G. Yang is with the Department of Wind and Energy Systems at the Technical University of Denmark, Anker Engelunds Vej 1, Bygning 101A, 2800 Kongens Lyngby, Denmark (e-mail: gygan@dtu.dk).

(CACRS)<sup>1</sup> [25]. So far, a consensus has not been reached on the most favorable current saturation strategies. The analysis of this paper applies to GFM IBRs equipped with CACRS. The transient stability of GFM IBRs with other CRS methods can be referred to [5], [21], [22], [26], [27].

Reference [28] presented a segmental equal area criterion for transient stability assessment of virtual synchronous generator (VSG) GFM IBRs equipped with CACRS. A Lyapunov-based method for transient stability analysis of GFM IBRs equipped with CACRS is provided in [29]. The existence of a saturated stable equilibrium point (satSEP) is pointed out in [28]–[30]. According to [30], if the angle of satSEP is more than the saturation threshold angle, the GFM IBR might be locked into the current-saturation mode through converging to satSEP. Nevertheless, as will be shown later in this paper, there exists another circumstance for converging to the satSEP. To explore circumstances in which a GFM IBR is locked into the satSEP, the conditions for entering and exiting the current-saturation mode should be identified. Reference [31] discussed that these two conditions are functions of the angle of the converter's reference dq-frame (local reference frame) from the grid's Thevenin voltage angle (common reference frame). Reference [31] also discussed that the set of angles for which the GFM IBR enters the current-saturation mode and the set of angles it exits are not complements of each other. In the rest of this paper, these two sets are mentioned as (a) the set of returning angles as the set of angles in which the voltage controller generates a current reference less than the allowable amount if it is in the current-saturated operation mode and (b) the set of entering angles as the set of angles in which the GFM IBR transits from normal operation mode, where the current limitation mechanism is not activated, to the current-saturation mode. Formulations for the set of entering angles have been extensively presented in the literature, e.g. in [4], [28]. However, an analytical approach for the set of returning angles has not been attempted.

To the best of our knowledge, a closed-form expression for the set of returning angles and a comprehensive analysis of the situations in which a GFM IBR is locked into the current-saturation mode after disturbances are missing in the literature. To bridge this gap, this paper first identifies conditions under which a GFM IBR returns from the current-saturation mode. All the circumstances under which a GFM IBR converges to the satSEP are also explored in this paper. All formulations and analyses provided in this paper are valid for different  $X/R$  ratios. The main contributions of this paper are:

- A formulation for the set of returning angles is derived. It is proven that this set is a function of the angle of the magnitude-saturated current (mentioned as the saturated current in the rest of the paper).
- The circumstances in which a GFM IBR is locked into the satSEP are investigated.
- The influence of various parameters, such as the saturated current angle and the  $X/R$  ratio of the grid impedance

on the post-fault recovery and the transient stability, is analyzed.

The rest of the paper is organized as follows. Section II presents a general overview of multi-loop VSG GFM IBRs. Section III formulates the situations in which a GFM IBR returns from the current-saturation mode. The causes of entering the current-saturation mode and the model of a GFM IBR in the current-saturation mode are also discussed in Section III. The model of transient stability of a VSG considering CACRS is provided in Section IV. Circumstances that a GFM IBR is locked into the current-saturation mode are also explored in Section IV. A sensitivity analysis on the effect of the grid's conditions and controller's parameters on transient stability is provided in Section V. The case studies are presented in Section VI followed by conclusions.

## II. SYSTEM STRUCTURE

There are several control structures for GFM IBRs in the literature. This paper considers a typical three-layer VSG as shown in Fig. 1 [4], [32], [26]. The inverter is connected to the grid, which is modeled as a Thevenin equivalent of voltage  $\vec{V}_g$  and impedance of  $R_g + jX_g$ , through a transformer with the impedance  $R_{tr} + jX_{tr}$  and an LC filter with inductance of  $L_f$  and capacitance of  $C$ . The total equivalent impedance from IBR terminal is  $(R_g + jX_g) + (R_{tr} + jX_{tr}) = R + jX = Ze^{j\phi}$ . Since the filter capacitance is small, its effect is neglected in the rest of the paper.

The inverter is controlled through a three-layer hierarchical control containing the outer layer, the inner layer, and the innermost layer shown with colors blue, purple, and green in Fig. 1, respectively. The outer layer consists of APC, which emulates the second order swing equation [33], and reactive power controller (RPC), which controls the reactive power by setting a reference magnitude for the voltage [2]. Since RPC is not the focus of this paper, it is not shown in Fig. 1, and we assume that it always generates the nominal voltage reference. APC generates the frequency and angle for the converter's reference dq-frame. The difference between the angle of the converter's (local) reference frame and the common reference frame ( $\delta := \theta - \theta_g$ ) is called APC angle, which plays a critical role in keeping the GFM IBR synchronous with the grid. The inputs to APC are  $P_0$  and  $P$ , which are, respectively, the active power reference and active power output. Active power output is calculated from measured voltage and current output. The inner controller includes the voltage controller which controls the terminal voltage  $\vec{V}$  to be aligned with the d-axis with the magnitude of  $V_d^{\text{ref}}$ . This controller generates the current reference for the current controller, which is the innermost control layer. The GFM IBR acts as a voltage source unless the magnitude of the current reference exceeds the threshold  $I_s^{\text{max}}$ . In this situation, the saturation block gives the saturated current reference to the current controller, and the GFM IBR behaves as a current source.

## III. CURRENT-SATURATION OPERATION MODE

In this section, the causes of entering the current-saturation mode and the corresponding modeling of a GFM IBR in the

<sup>1</sup>Constant angle in this context means a fixed angle from the local reference frame. This angle might vary from the common reference frame.

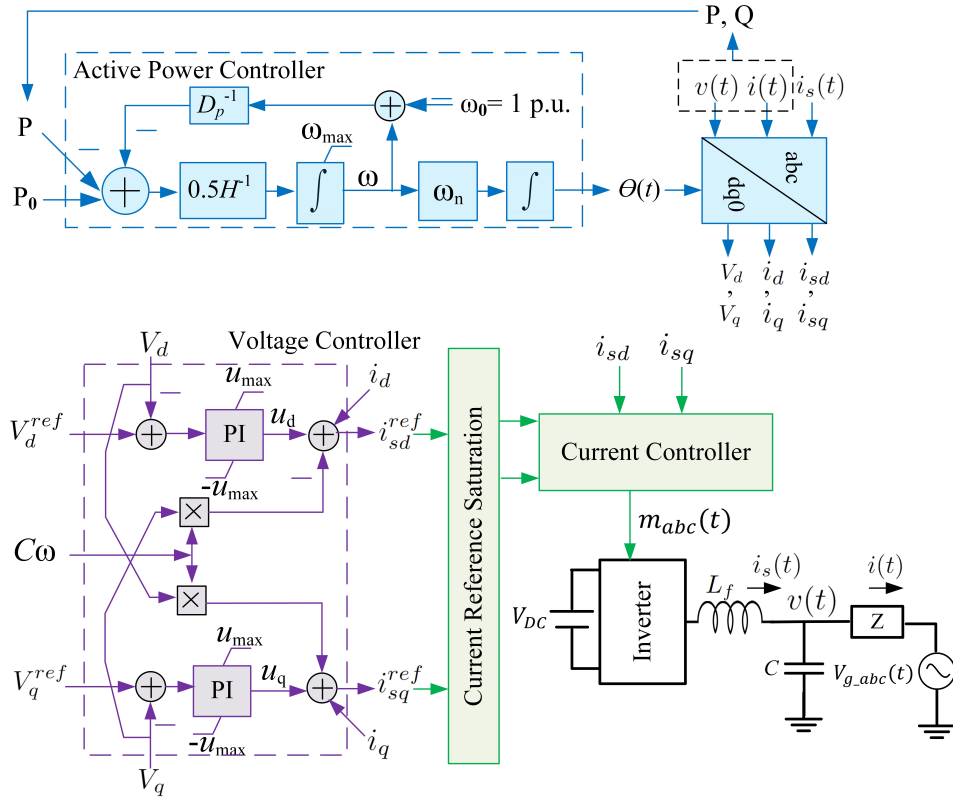


Fig. 1. The structure of a three-layer VSG GFM IBR [4], [26], [32].

current-saturation mode are detailed. Then, a mathematical expression for the set of APC angles in which the GFM IBR returns to the normal operation mode is derived. This is followed by analyzing the operation mode of GFM IBRs for different APC angles.

When a GFM IBR operates in the normal operation mode, its terminal voltage aligns with the d-axis and has the magnitude of  $V_d^{\text{ref}}$  as shown in Fig. 2(a). In this situation, the active power output is expressed as

$$P_{\text{unsat}} = \frac{(V_d^{\text{ref}})^2}{Z} \sin \alpha + \frac{V_g V_d^{\text{ref}}}{Z} \sin(\delta - \alpha) \quad (1)$$

where  $\delta = \theta(t) - \theta_g(t)$  is the APC angle, which is the angle between the converter's dq-frame and grid's Thevenin voltage, and  $\alpha = \arctan(R/X) = 90^\circ - \phi$ . If there is a deep voltage sag Fig. 2(b) or excessive APC angle Fig. 2(c), the GFM IBR is no longer able to regulate the terminal voltage to  $\vec{V}_{\text{ref}} = (V_d^{\text{ref}}, 0)$  subject to the current limit [4], [29]. Therefore, a current limitation mechanism is needed to limit the current. In this paper, the studied current limitation mechanism is CACRS, in which the angle of saturated current is constant from the local (converter's) reference frame. When the magnitude of the current reference generated by the voltage controller surpasses the limitation, the saturation block gives the saturated current reference  $(\vec{i}_{sd}^{\text{ref}}, \vec{i}_{sq}^{\text{ref}}) = (I_s^{\text{max}} \cos \beta, I_s^{\text{max}} \sin \beta)$  to the current controller, where  $\beta$  is the saturated current angle with respect to the converter's reference d-axis [30]. In this situation,  $(V_d, V_q) \neq (V_d^{\text{ref}}, 0)$  as depicted in Fig. 2 (d). Neglecting the impact of the filter capacitor, according to kirchhoff's voltage

law the terminal voltage in the current-saturation mode in the local reference frame is

$$V_d^{\text{sat}} + jV_q^{\text{sat}} = V_g e^{-j\delta} + I_s^{\text{max}} e^{j\beta} Z e^{j(\frac{\pi}{2} - \alpha)}. \quad (2)$$

After separating the real and imaginary parts of (2), the terminal voltage of the IBR under the converter's reference dq-frame is calculated as

$$V_d^{\text{sat}} = V_g \cos \delta + Z I_s^{\text{max}} \sin(\alpha - \beta) \quad (3)$$

$$V_q^{\text{sat}} = -V_g \sin \delta + Z I_s^{\text{max}} \cos(\alpha - \beta). \quad (4)$$

Since the terminal voltage of the GFM IBR is no longer aligned with the d-axis of the local reference frame in the current-saturation mode, the current angle  $\beta$  no longer naturally reflects the power factor. Instead, the power factor angle is  $\arctan(V_q^{\text{sat}}/V_d^{\text{sat}}) - \beta$ .

The active power output during the current-saturation operation mode is

$$P_{\text{sat}} = R(I_s^{\text{max}})^2 + V_g I_s^{\text{max}} \cos(\delta + \beta) \quad (5)$$

which depends on both  $\delta$  and  $\beta$ . Hence, the selection of  $\beta$  significantly impacts the transient behavior and therefore the stability of a GFM IBR, which will be detailed later in Sections IV and V.

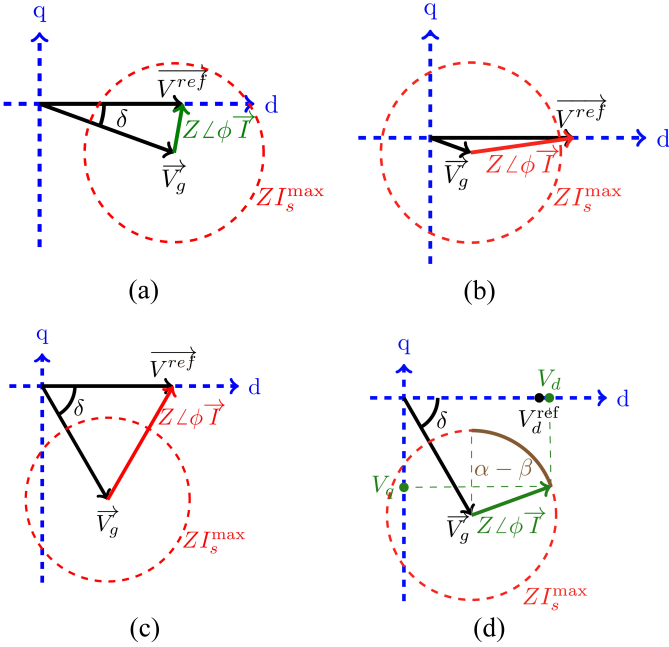


Fig. 2. Phasor-Diagram of the voltages in (a) steady-state normal operation mode, (b) voltage sag, (c) extra APC angle, and (d) extra APC angle with CRS.

#### A. Sets of Entering and Returning Angles

The GFM IBR enters the current-saturation mode [4], [26], [28] if

$$\cos \delta \leq \frac{1}{2} \left( \frac{V_d^{\text{ref}}}{V_g} + \frac{V_g}{V_d^{\text{ref}}} - \frac{(ZI_s^{\text{max}})^2}{V_g V_d^{\text{ref}}} \right). \quad (6)$$

Defining the saturation threshold angle as

$$\delta_{\text{sat}} := \arccos \left( \frac{1}{2} \left( \frac{V_d^{\text{ref}}}{V_g} + \frac{V_g}{V_d^{\text{ref}}} - \frac{(ZI_s^{\text{max}})^2}{V_g V_d^{\text{ref}}} \right) \right), \quad (7)$$

the set of entering angles (denoted  $\mathcal{S}$ ) where the APC angle satisfying the condition (6), is given by

$$\mathcal{S} = [-180^\circ, -\delta_{\text{sat}}] \cup [\delta_{\text{sat}}, 180^\circ]. \quad (8)$$

This means a GFM IBR enters the current-saturation mode if the absolute value of the APC angle  $\delta$  exceeds a threshold. This threshold depends on the grid voltage as analyzed in [4], [28] in detail.

As soon as the APC angle exits  $\mathcal{S}$ , the voltage controller of GFM IBR should generate a current reference less than the maximum allowable value, and the GFM IBR should come back to the normal operation mode. However, this may not be true under certain circumstances. The set of APC angles at which the GFM IBR can return to the normal operation mode spontaneously is expressed as

$$\mathcal{R} := \left\{ -180^\circ \leq \delta \leq 180^\circ \mid (i_{sd}^{\text{ref}})^2 + (i_{sq}^{\text{ref}})^2 \leq (I_s^{\text{max}})^2 \right\} \quad (9)$$

where  $i_{sd}^{\text{ref}}$  and  $i_{sq}^{\text{ref}}$  are functions of the terminal voltage, which is, in turn, a function of  $\delta$ . These two references are unsaturated immediate outputs of the voltage controller.

One of the main goals of this work is to delve into  $\mathcal{R}(\beta)$  by solving (9). The current reference generated by the voltage controller is given by [32]:

$$i_{sd}^{\text{ref}} = u_d - yV_q + i_d \approx u_d + I_s^{\text{max}} \cos \beta \quad (10)$$

$$i_{sq}^{\text{ref}} = u_q + yV_d + i_q \approx u_q + I_s^{\text{max}} \sin \beta \quad (11)$$

where  $y = C\omega$  is the filter shunt admittance, and  $u_d$  and  $u_q$  are the outputs of the PI voltage controller depicted in Fig. 1. In the normal operation mode, the output of the PI controller are  $u_d = C \frac{dV_d}{dt}$  and  $u_q = C \frac{dV_q}{dt}$  [32]. Therefore, these two variables are zero in the steady-state of the normal operation mode. By substituting (10) and (11), into (9), it can be rewritten as

$$(u_d + I_s^{\text{max}} \cos \beta)^2 + (u_q + I_s^{\text{max}} \sin \beta)^2 \leq (I_s^{\text{max}})^2. \quad (12)$$

This is equivalent to

$$2u_d I_s^{\text{max}} \cos \beta + 2u_q I_s^{\text{max}} \sin \beta + u_d^2 + u_q^2 \leq 0. \quad (13)$$

The output of the PI controllers of the voltage controller is limited between  $-u_{\text{max}}$  and  $u_{\text{max}}$  [22], [26]. Inside the PI controller block the clamping anti-windup method is employed to prevent the integrator from windup when the output of the block reaches its limits [22], [26], [34]. In the current-saturation mode, voltage error signals  $V_d^{\text{ref}} - V_d$  and  $V_q^{\text{ref}} - V_q$  are non-zero because the voltage is not regulated. Since the PI controllers are fast, they quickly reach their limitations upon the exposure to a sustained positive or negative error signal. Therefore,  $u_d$  and  $u_q$  are either  $u_{\text{max}}$  or  $-u_{\text{max}}$  depending on the sign of the voltage error signals  $V_d^{\text{ref}} - V_d$  and  $V_q^{\text{ref}} - V_q$  where  $V_q^{\text{ref}} = 0$ . Therefore, equation (13), which is the condition for returning to the normal operation mode, can be rewritten as

$$2u_{\text{max}} \text{sign}(u_d) I_s^{\text{max}} \cos \beta + 2u_{\text{max}} \text{sign}(u_q) I_s^{\text{max}} \sin \beta \leq -2u_{\text{max}}^2, \quad (14)$$

which is equivalent to

$$\text{sign}(u_d) \cos \beta + \text{sign}(u_q) \sin \beta \leq -\frac{u_{\text{max}}}{I_s^{\text{max}}}. \quad (15)$$

$u_{\text{max}}$  should be small in order to prevent a large rate of change of  $V_d$  and  $V_q$ , which cause a huge transient in the capacitor's current. If  $u_{\text{max}} \ll I_s^{\text{max}}$ , the right-hand side of (15) is close to zero. The set of the saturated current angle  $\beta$ , which satisfies (15), is presented in Table I.

According to Table I, for  $-45^\circ \leq \beta \leq 0^\circ$ , (15) is satisfied if  $u_d$  is negative. Signals  $u_d$  and  $u_q$  have the same signs with the voltage controller's error signals, i.e.,  $V_d^{\text{ref}} - V_d$  and

TABLE I  
THE SETS OF  $\beta$  SATISFYING (15)

	$\text{sign}(u_d) > 0$	$\text{sign}(u_d) < 0$
$\text{sign}(u_q) > 0$	$-90^\circ \leq \beta \leq -45^\circ$	$-90^\circ \leq \beta \leq 0^\circ$
$\text{sign}(u_q) < 0$	$\emptyset$	$-45^\circ \leq \beta \leq 0^\circ$

$-V_q$ , respectively. According to (3),  $V_d^{\text{ref}} - V_d$  is negative if  $-\delta_d^p(\beta) \leq \delta \leq \delta_d^p(\beta)$ , where  $\delta_d^p(\beta)$  is defined as

$$\delta_d^p(\beta) = \arccos\left(\frac{V_d^{\text{ref}} - ZI_s^{\text{max}} \sin(\alpha - \beta)}{V_g}\right). \quad (16)$$

$\delta_d^p(\beta)$  is the maximum APC angle such that  $V_d^{\text{ref}} \leq V_d$ . On the other hand, for  $-90^\circ \leq \beta \leq -45^\circ$ , (15) is satisfied if  $u_q$  is positive, which means  $-V_q > 0$ . According to (4), this is equivalent to  $\delta_q^p(\beta) \leq \delta \leq 180^\circ - \delta_q^p(\beta)$ , where  $\delta_q^p(\beta)$  is defined as

$$\delta_q^p(\beta) = \arcsin\left(\frac{ZI_s^{\text{max}} \cos(\alpha - \beta)}{V_g}\right). \quad (17)$$

$\delta_q^p(\beta)$  is the minimum APC angle such that  $V_q \leq 0$ . Therefore,  $\mathcal{R}$  depends on  $\beta$ , that is,

$$\mathcal{R}(\beta) = \begin{cases} [-\delta_d^p(\beta), \delta_d^p(\beta)], & \text{if } \beta \in [-45^\circ, 0^\circ] \\ [\delta_q^p(\beta), 180^\circ - \delta_q^p(\beta)], & \text{if } \beta \in [-90^\circ, -45^\circ]. \end{cases} \quad (18)$$

To reveal the rationale behind (18), a comparison between the current reference and maximum allowed current for different ranges of  $\beta$  is conducted. When  $\beta \in [-45^\circ, 0^\circ]$ , the dominant component of the current reference is  $i_{sd}^{\text{ref}}$ , which is positive. When APC angle  $\delta$  enters the interval  $[-\delta_d^p(\beta), \delta_d^p(\beta)]$ , the sign of the d-component of voltage error becomes negative, therefore  $u_d$  becomes negative. As a result, the magnitude of the current reference becomes smaller than the maximum value according to (10) and (12). When  $\beta \in [-90^\circ, -45^\circ]$ ,  $i_{sq}^{\text{ref}}$ , which is negative, is the dominant component of the current reference. As soon as  $\delta$  enters the interval  $[\delta_q^p(\beta), 180^\circ - \delta_q^p(\beta)]$ , the q-component of voltage error and, consequently,  $u_q$  become positive. Therefore, the magnitude of the current reference becomes smaller than the maximum value according to (11) and (12).

Fig. 3 shows the variation of  $\mathcal{R}$  and  $\mathcal{S}$ .  $\mathcal{R}$  is a function of  $\beta$  whereas  $\mathcal{S}$  is independent from  $\beta$ . This is because while the GFM IBR is in the normal operation mode, the voltage error does not depend on the saturated current angle. Therefore,  $\beta$  does not affect the current reference generated by the voltage controller in normal operation mode. Nevertheless, as soon as the GFM IBR enters the current-saturation mode, voltage error highly depends on the saturated current angle. Hence,  $\beta$  significantly affects the magnitude of the current reference generated by the voltage controller. As depicted in Fig. 3, set of entering angles equals the set of angles in which  $V_d^{\text{ref}} \leq V_d$  if  $-45^\circ < \beta < 0$ , and it is the set of angles in which  $V_q \leq 0$  if  $-90^\circ < \beta < -45^\circ$ . This set is depicted with the hatched area in this figure. The filled area in Fig. 3 visualizes the set of entering angles.

Depending on the APC angle, the GFM IBR might exhibit four different post-fault behaviors:

- $\delta \in \mathcal{S} - \mathcal{R}(\beta)$ : The GFM IBR operates in the current-saturation mode [31]. It is shown with the solid-filled area in Fig. 3.
- $\delta \in \mathcal{R}(\beta) - \mathcal{S}$ : The GFM IBR operates in the normal operation mode [31]. The unfilled hatched area in Fig. 3 represents this subset.

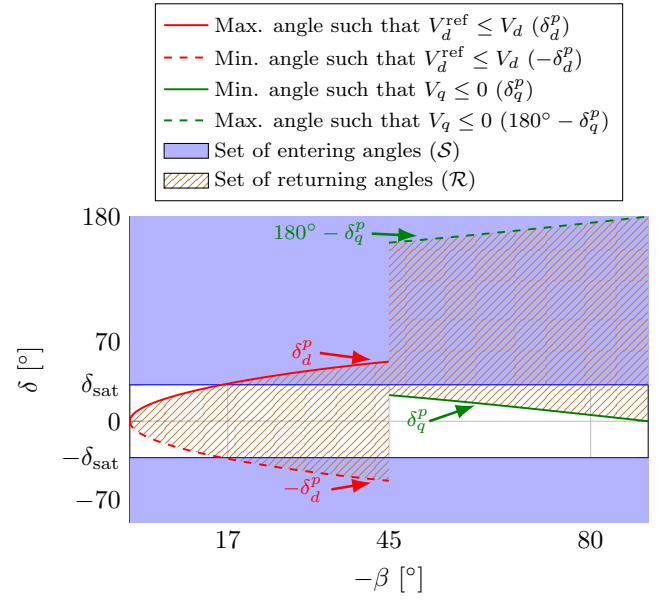


Fig. 3. Illustration of entering and returning sets represented by the solid and hatched fill areas, respectively. Here,  $Z = 0.46$  p.u. and  $X/R = \infty$ .

- $\delta \in \mathcal{R}(\beta) \cap \mathcal{S}$ : The GFM IBR oscillates between normal operation and current-saturation modes [31]. This subset is shown as the intersection of the solid-filled area and hatched area in Fig. 3. These oscillations can be reduced using the forced saturation introduced in [4].
- $\delta \notin \mathcal{R}(\beta) \cup \mathcal{S}$ : The GFM IBR retains its mode. The white area in Fig. 3 represents this situation. If the GFM IBR was already in the current-saturation mode, it remains in the current-saturation mode even though the post-disturbance APC angle  $\delta_{af} \notin \mathcal{S}$ .

#### IV. TRANSIENT STABILITY OF GFM IBRS

The GFM IBR synchronizes itself to the grid through APC, which follows the second-order swing equation [33] if it is designed as a VSG:

$$P_0 - P = 2H \frac{d\omega}{dt} + \frac{1}{D_p} (\omega - \omega_0) \quad (19)$$

$$\frac{d\delta}{dt} = \omega_n (\omega - \omega_0) \quad (20)$$

where  $H$ ,  $D_p$ ,  $P_0$ ,  $\omega_0$ , and  $\omega_n$  are virtual inertia, active droop coefficient, active power reference, set-point frequency, and the nominal frequency, respectively. These equations outline the strong tie between the trajectory of the APC and the active power, which follows (1) and (5) for the normal and the current-saturation operation modes, respectively. The intersections of the power-angle curve and the power reference, shown in Fig. 4, form equilibrium points which are:

- SEP: This is the normal stable equilibrium point to which convergence is desired. Deduced from (1), it is calculated

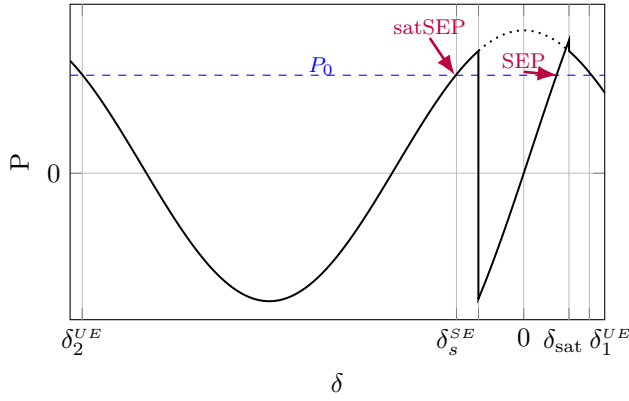


Fig. 4. Power-Angle curve for a GFM IBR equipped with the CRS.

as

$$\delta^{SE} = \alpha + \arcsin \left( \frac{Z}{V_g V_d^{\text{ref}}} \left( P_0 - \frac{(V_d^{\text{ref}})^2}{Z} \sin \alpha \right) \right). \quad (21)$$

- Unstable Equilibrium 1 ( $\delta_1^{UE}$ ): If the APC angle reaches this value while  $\omega > \omega_0$ , the GFM IBR loses its synchronism with the grid. Based on (5), it is calculated as

$$\delta_1^{UE}(\beta) = -\beta + \arccos \left( \frac{P_0 - R(I_s^{\text{max}})^2}{V_g I_s^{\text{max}}} \right). \quad (22)$$

It shows that decreasing  $\beta$  increases the  $\delta_1^{UE}(\beta)$  which enhances transient stability by pushing away the unstable equilibrium point.

- Unstable Equilibrium 2 ( $\delta_2^{UE}(\beta)$ ): The GFM IBR loses its synchronism if the APC angle reaches this value while  $\omega < \omega_0$ . According to (5), this angle is calculated as

$$\delta_2^{UE}(\beta) = \delta_1^{UE}(\beta) - 360^\circ. \quad (23)$$

This equilibrium point is unlikely to be reached in practice except in some adverse situations, e.g. dramatic phase jump.

- satSEP ( $\delta_s^{SE}(\beta)$ ): It is the stable intersection between the power reference and power output in the current-saturation mode. Deduced from (5), it is calculated as

$$\delta_s^{SE}(\beta) = -\beta - \arccos \left( \frac{P_0 - R(I_s^{\text{max}})^2}{V_g I_s^{\text{max}}} \right). \quad (24)$$

It has been discussed in [30] that if  $\delta_{\text{sat}} \leq \delta_s^{SE}(\beta)$ , the satSEP has a DOA that causes locking in the saturation mode. It will be discussed in the following subsection that there is another condition for locking into the saturation mode. Notice that since the power-angle curves are trigonometric functions, the equilibrium points repeat themselves every  $360^\circ$ . Hence, it is theoretically possible that a GFM IBR converges to another stable equilibrium point after passing an unstable equilibrium point. However, the power output becomes negative in a wide range of angles before it converges to a far stable equilibrium point. Such negative power might cause DC link capacitor

over-voltage, which may trip the protection. Therefore, we only focus on analyzing the behavior of GFM IBR between the two closest unstable equilibrium points.

#### A. Converging to the Saturated Stable Equilibrium Point

A GFM IBR is locked into the current-saturation mode if it converges to the satSEP. It has been shown in [30] that if  $\delta_s^{SE}(\beta) \in \mathcal{S}$  while the post-fault APC angle  $\delta_{af} \in \mathcal{S}$ , the post-fault trajectory might converge to the satSEP. However, such condition, which is denoted as  $\mathcal{C}_1$  here, is not necessary for the convergence to the satSEP. Since the set of returning angles  $\mathcal{R}(\beta)$  is not exactly the complement of  $\mathcal{S}$ , there are cases that even though  $\delta_s^{SE}(\beta) \notin \mathcal{S}$ , the GFM IBR cannot escape from the current-saturation mode. It happens if the APC angle does not enter  $\mathcal{R}(\beta)$  during its post-disturbance trajectory until converging to satSEP. Notice that in this condition it does not matter whether the APC angle trajectory is inside or out of  $\mathcal{S}$ . Since it does not enter  $\mathcal{R}(\beta)$  it stays in the current saturation mode. This circumstance is denoted as  $\mathcal{C}_2$  here as the combination of the following conditions: (a)  $\delta_s^{SE}(\beta) \notin \mathcal{R}(\beta) \cup \mathcal{S}$ , (b) the post-fault trajectory toward  $\delta_s^{SE}(\beta)$  does not enter the set of returning angles  $\mathcal{R}(\beta)$ , and (c) the GFM IBR does not lose synchronism with the grid. This set of conditions is expressed as

$$\mathcal{C}_2 : \begin{cases} \delta_s^{SE}(\beta) \notin \mathcal{R}(\beta) \cup \mathcal{S} & (\mathcal{C}_{21}) \\ \delta(t) \notin \mathcal{R}(\beta), \forall t & (\mathcal{C}_{22}) \\ \delta_2^{UE}(\beta) < \delta(t) < \delta_1^{UE}(\beta), \forall t & (\mathcal{C}_{23}) \end{cases} \quad (25)$$

where  $\mathcal{C}_{21}$  is a static condition,  $\mathcal{C}_{22}$  and  $\mathcal{C}_{23}$  are dynamic conditions.

Figs. 5 and 6 depict two examples of converging to the satSEP for a GFM IBR with  $D_p = 0.03$  p.u. connected to a Grid with the equivalent impedance of  $Z = 0.46$  p.u. and  $X/R = 20$ . In these figures, the solid-filled area represents

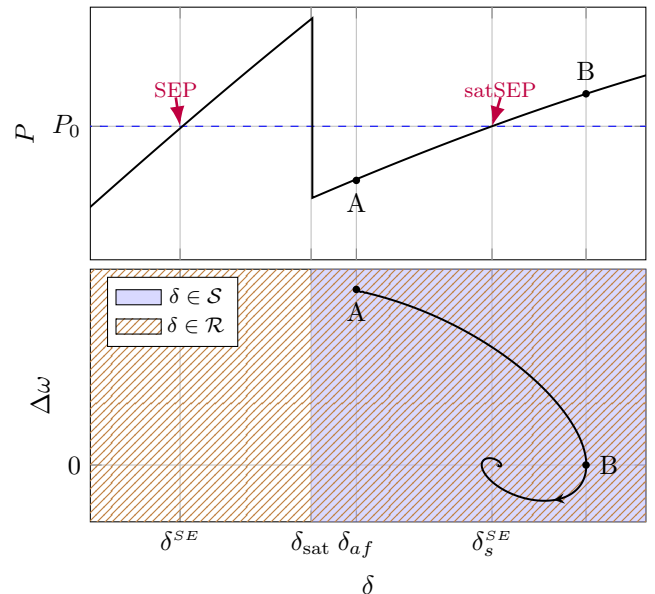


Fig. 5. Post-fault trajectory and active power for the case where  $\mathcal{C}_1$  holds.

the  $S$  and the hatched area represents  $\mathcal{R}(\beta)$ . The GFM IBR is forced to be in the current-saturation mode if  $\delta \in S \cap \mathcal{R}(\beta)$  as it was proposed in [4]. The convergence to the satSEP in Fig. 5 is due to  $\mathcal{C}_1$ . In this case, the satSEP belongs to the set of entering to saturation angles and contains point A in its DOA. On the other hand,  $\mathcal{C}_2$  is the cause of locking into the saturation mode in Fig. 6. In this example, the satSEP is out of  $S$ . However, since the post-fault angle ( $\delta_D$ ) is out of  $\mathcal{R}(\beta)$ , the GFM IBR does not come back to the normal operation mode. The remainder of its post-fault trajectory does not pass any point in  $\mathcal{R}(\beta)$  until it converges to the satSEP. According to Fig. 6, the GFM IBR does not converge to the SEP even though the post-fault state D is close to SEP. The fulfillment of condition  $\mathcal{C}_2$  imposes a significant challenge as even relatively small disturbances might also lead to undesired consequences.

As discussed earlier in this section, risk of convergence to the satSEP highly depends on the value of  $\delta_s^{SE}(\beta)$  and  $\mathcal{R}(\beta)$ , which are functions of the saturated current angle  $\beta$ , the proper selection of  $\beta$  can eliminate the risk of locking into the current-saturation mode through  $\mathcal{C}_1$  or  $\mathcal{C}_2$ . If the sufficient condition  $\delta_s^{SE}(\beta) \in \mathcal{R}(\beta) - S$  is met, the GFM IBR is not locked into the current-saturation mode. This is because of the fact that the GFM IBR comes back to the normal operation mode at the angle of satSEP.  $\delta_s^{SE}(\beta)$  depends on the power reference in addition to  $\beta$  as demonstrated in Fig. 7. Therefore,  $\beta$  satisfying the mentioned condition differs for different power references. Hence, an adaptive  $\beta$  selection is needed to mitigate or decrease the risk of converging to the satSEP.

To avoid the complexity in Section V, it is assumed that  $\mathcal{R}(\beta)$  and  $S$  are complements. Therefore, condition  $\mathcal{C}_2$  is not analyzed in Section V. This assumption is made only in that section. Later, cases that these two sets are not complements

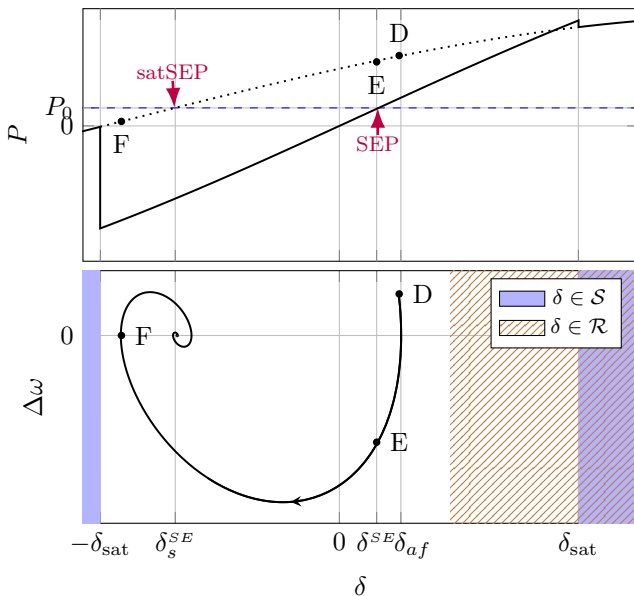


Fig. 6. Post-fault trajectory and active power output for a scenario that condition  $\mathcal{C}_2$  meets. The dotted curve is the power output in the current-saturation mode while  $\delta \notin S$ .

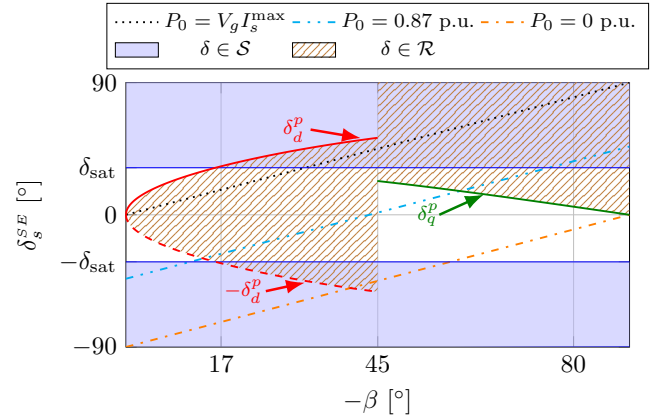


Fig. 7. Relation between the satSEP angle and  $\beta$ . Solid filled area represents  $S$  and hatched area shows  $\mathcal{R}(\beta)$ .

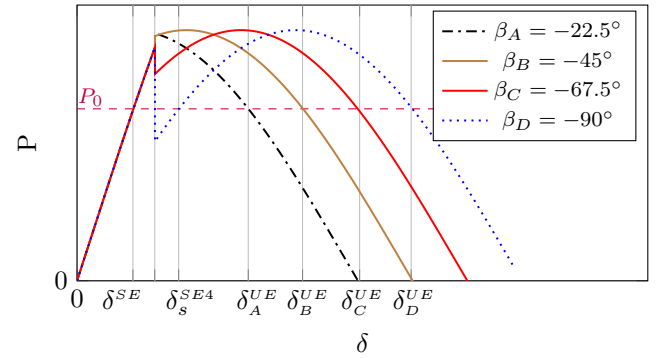


Fig. 8. Power-Angle curves for different saturated current angles  $\beta$ .

are analyzed in the Case Study section.

## V. EFFECT OF PARAMETERS ON TRANSIENT STABILITY

It has been discussed in [4] that the current saturation deteriorates the post-fault transient stability by decreasing the acceleration area and the angle of the unstable equilibrium point 1. This decrement depends on  $\beta$  in addition to APC control parameters and grid parameters because  $\beta$  affects the active power-angle curve as demonstrated in Fig. 8. This figure depicts that a smaller  $\beta$  leads to a shift in unstable equilibrium point 1 and an increase in deceleration area compared to a bigger  $\beta$ . However, if  $\beta$  exceeds a lower limit, there exists an satSEP in  $S$ , which might cause locking in the current-saturation mode through the condition  $\mathcal{C}_1$ .

Fig. 9 shows post-disturbance transient phase portraits for different saturated current angles.  $\beta$  is zero in Fig. 9(a). The satSEP attracts a subset of the state-space under the condition  $\mathcal{C}_1$ . In Fig. 9(b),  $\beta$  is  $-45^\circ$ . Thus, the satSEP is out of  $S$ , and  $\mathcal{C}_1$  cannot hold. The DOA of SEP is considerably bigger than that of Fig. 9(a). The saturated current angle is  $-90^\circ$  in Fig. 9(c). As depicted in this phase portrait, DOA of the satSEP is considerably bigger than DOA of the SEP. If the droop coefficient increases from 0.03 p.u. to 0.09 p.u., the DOAs of these two equilibrium points become hardly separable as

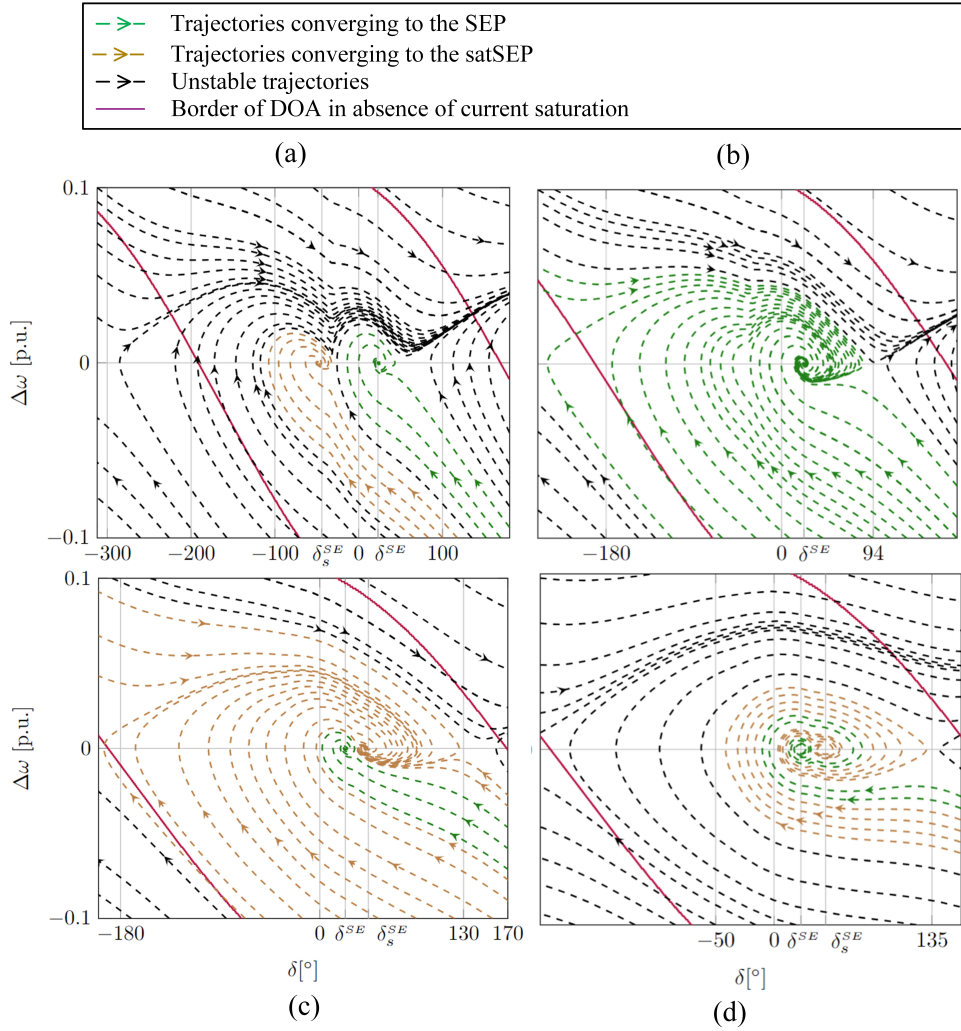


Fig. 9. Phase portraits for a GFM IBR connected to an equivalent impedance of  $Z = 0.46$  p.u., and  $X/R = 10$ , and  $\beta$  equals to (a)  $0^\circ$ , (b)  $-45^\circ$ , (c)  $-90^\circ$ , and (d)  $-90^\circ$ .  $D_p$  equals to 0.03 p.u. for (a)-(c) and 0.09 p.u. for (d). Purple lines are borders of DOA for unsaturated GFM IBRs. Green lines and brown lines are trajectories converging to the SEP and the satSEP, respectively.

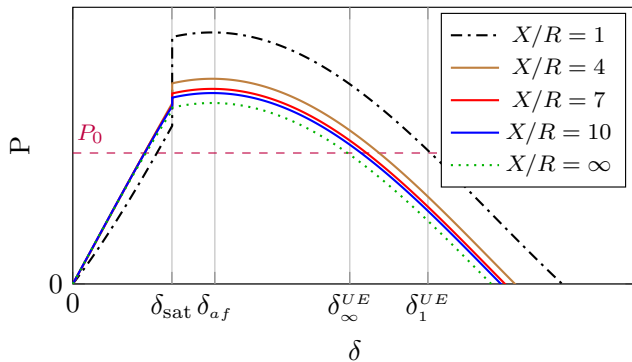


Fig. 10. Power angle curves for different  $X/R$  ratios. The GFM IBR is connected to an equivalent impedance of 0.46 p.u., and  $D_p = 0.03$  p.u.

shown in Fig. 9(d). Therefore, it is crucial to set  $\beta$  in a way to exclude the satSEP from  $\mathcal{S}$ . So that the condition  $\mathcal{C}_1$  is not met.

Other main effecting parameters are the droop coefficient,  $X/R$  ratio, and the total impedance  $Z$ , which are analyzed in detail in the rest of this section. All DOAs are assessed through the numerical calculation of trajectories based on the swing equation and saturated and unsaturated active powers.  $\beta$  in these cases is  $-45^\circ$  so that condition  $\mathcal{C}_1$  does not hold.

Decreasing the droop coefficient provides more damping to the swing equation (19). Therefore, an expanded DOA is expected [13]. The total impedance  $Z$  and  $X/R$  ratio shape the relation between the power and angle. Therefore, they influence the dynamics of APC. Fig. 10 depicts that the power output in the current-saturation mode is more for resistive grid impedance compared to inductive grids. This difference accounts for the active power losses. Furthermore, the unstable equilibrium point 1 is shifted away. Therefore, the GFM IBR exhibit better transient stability when it is connected to a more resistive grid. The DOA of the SEP when the GFM IBR is connected to a weaker grid (larger amount of impedance) is smaller compared to those connected to stronger grids according to Fig. 11.



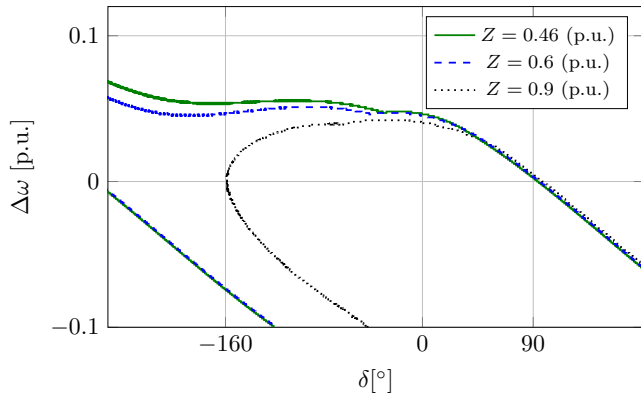


Fig. 11. Borders of DOAs for different total impedances.  $X/R = 10$ , and  $D_p = 0.03$  p.u.

TABLE II  
PARAMETERS OF THE SIMULATED GFM FARM.

Param.	Values	Units	Descriptions
$S_b$	310	MVA	Nominal apparent power
$V_b$	400	V	Nominal Voltage
$V_{dc}$	1200	V	DC link voltage
$n$	816	-	Number of identical parallel GFM IBRs
$f_n$	60	Hz	Nominal frequency
$D_p$	0.03	p.u.	Active droop coefficient
$H$	2	p.u.	Virtual inertia
$\Delta\omega_{\max}$	0.0066	p.u.	Maximum frequency deviation
$V_d^{\text{ref}}$	1	p.u.	Voltage reference magnitude
$I_s^{\max}$	1.2	p.u.	Maximum allowed current
$X_{tr}$	0.16	p.u.	Total reactance of transformer windings
$u_{\max}$	0.063	p.u.	Max. output of the voltage PI controller

## VI. CASE STUDIES

To examine the analyses provided in the previous sections, the system of Fig. 1 with the general parameters of Table. II [4] is simulated in Simulink/MATLAB [35]. Since the GFM IBRs are parallel in the same bus, with the same sharing of loading, and identical, they can be modeled as an equivalent GFM IBR [36]. If the IBRs were not identical and in the same location, the analysis of this GFM farm would be more complicated. It is connected to a grid with the post-fault Thevenin impedance of 0.3 p.u. and  $X/R$  ratio of 20 (totally,  $Z = 0.46$  p.u.). Eight cases are simulated. In all cases, the system is assumed to be exposed to a three-phase short-circuit fault, which is modeled as a voltage drop of 0.95 p.u. until reaching the post-fault angle  $\delta_{af}$  right after clearing the fault. These cases are listed in Table. III.

Cases A, B, and C are compared to each other to demonstrate the effect of  $\beta$  on post-fault recovery and transient stability.  $\beta$  and the parameters that depend on  $\beta$  are different for these three cases as mentioned in Table. III. Cases D and E are compared to each other to investigate the risk of locking in the current-saturation mode through  $\mathcal{C}_2$ , explained in Subsection. IV-A when the post-fault angle is out of  $\mathcal{R} \cup \mathcal{S}$ .  $\beta$  is the same for these two cases; however, fault duration and  $\delta_{af}$  are different. Case D is exposed to a longer duration of fault to reach the bigger post-fault angle  $\delta_{af}$  right after

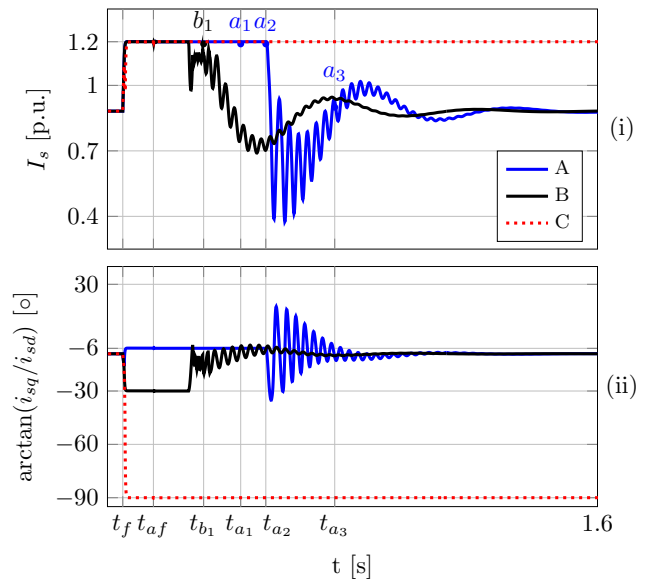


Fig. 12. Simulation results for the post-fault currents in Cases A, B, and C.

clearing the fault. Cases F, G, and H are compared to show a reduction in DOA caused by the current saturation.  $\beta$  and all other parameters are identical for Cases F and G. However, the fault duration for case G is longer. The post-fault angle  $\delta_{af}$  for Cases F and G are inside and outside the DOA, respectively. Fault duration in Case H is larger than F and G, and the GFM IBR's current is not limited. Case H is simulated to demonstrate the transient stability of the GFM IBR in the absence of current saturation. Since the grid impedance is the same for all cases, the set of entering angles, which is  $\mathcal{S} = [-180^\circ, -32.0455^\circ] \cup [32.0455^\circ, 180^\circ]$ , is identical for all of them except Case H, which is unsaturated. The parameters that get different values in each group of compared cases are in bold. For all these cases, fault started at  $t_f = 0.05$  s. Detailed analyses of these cases are provided in the rest of this section.

According to Fig. 12(i), the inverter's output current is limited to 1.2 p.u. for three Cases A, B, and C. After fault occurrence at  $t_f = 0.05$  s, the active power output drops to near zero. Therefore, the GFM IBR accelerates until clearing fault at  $t_{af} = 0.15$  s to the post-fault angle of  $\delta_{af} = 34.93^\circ$ . Among the three post-fault trajectories for these cases, Case B exhibits the fastest convergence to the SEP as illustrated in Fig. 13(i). The GFM IBR converges to the satSEP in the Case C because  $\delta_s^{SE}(\beta_C) = 44.52^\circ \in \mathcal{S}$ , and the initial point is within the satSEP's DOA. Since the GFM IBR is locked in the current-saturation mode, it cannot regulate the terminal voltage as shown in Fig. 13(iii). In Case A, theoretically based on (18),  $\mathcal{R}(\beta_A) = [-23.14^\circ, 23.14^\circ]$  and  $\mathcal{S} = [-180^\circ, -32.0455^\circ] \cup [32.0455^\circ, 180^\circ]$ . Therefore, after the fault is cleared, it stays in the current-saturation mode until the APC angle becomes less than  $23.14^\circ$  at  $t = 0.517$  s. In other words, the GFM IBR's APC angle is in  $\mathcal{S}$  right after the fault is cleared at  $t = 0.15$  s. It exits this set at  $t = 0.435$  s, shown as point  $a_1$  in Fig. 12(i) and Fig. 13(i). Since the GFM IBR enters  $\mathcal{R}(\beta_A) \cup \mathcal{S}$ , it retains its mode,

TABLE III  
 SIMULATED CASES.

Case	$P_0$	Fault duration [ms]	$\delta_0 [^\circ]$	$\delta_{af} [^\circ]$	$\beta [^\circ]$	$\mathcal{R} [^\circ]$	$\delta_s^{SE}$	$\delta_1^{UE} [^\circ]$
A	270 MW (0.87 p.u.)	100	23.38	34.93	<b>-6</b>	<b>[-23.14, 23.14]</b>	<b>-39.78</b>	<b>51.78</b>
B	270 MW	100	23.38	34.93	<b>-30</b>	<b>[-45.2, 45.2]</b>	<b>-15.77</b>	<b>75.78</b>
C	270 MW	100	23.38	34.93	<b>-90</b>	<b>[-1.3, 181.3]</b>	<b>44.22</b>	<b>135.78</b>
D	62 MW (0.2 p.u.)	<b>600</b>	5.23	<b>44.76</b>	-60	[14.84, 165.16]	-22.00	142.00
E	62 MW	<b>100</b>	5.23	<b>7.93</b>	-60	[14.84, 165.16]	-22.00	142.00
F	270 MW (0.87 p.u.)	<b>290</b>	23.38	<b>62.01</b>	-30	[-45.2, 45.2]	-15.77	75.78
G	270 MW	<b>330</b>	23.38	<b>67.71</b>	-30	[-45.2, 45.2]	-15.77	75.78
H	270 MW	<b>400</b>	23.38	<b>76.10</b>	<b>No current saturation implemented</b>			

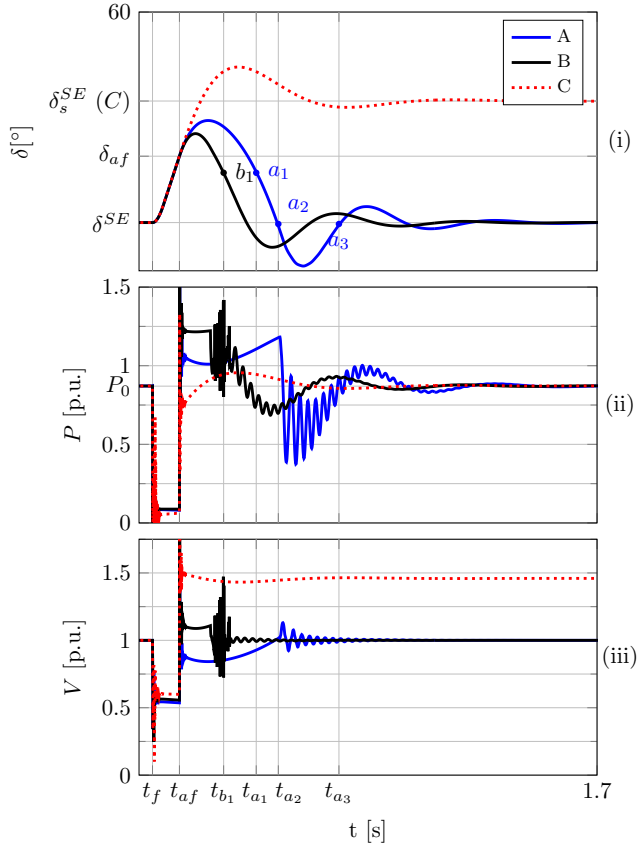


Fig. 13. Simulation results for the (i) angles, (ii) powers, and (iii) voltages in Cases A, B, and C.

i.e., the current-saturation mode. It returns to normal operation mode upon entrance to  $\mathcal{R}(\beta_A) - \mathcal{S}$  at  $t_{a_2} = 0.517$ s, shown as point  $a_2$  in Fig. 12(i) and Fig. 13(i). It enters the  $\mathcal{R}(\beta_A) \cup \mathcal{S}$  again at  $t_{a_3} = 0.742$  s, shown as  $a_3$  in Fig. 12(i) and Fig. 13(i). It retains its normal operation mode. Since it never again enters  $\mathcal{S}$  during its trajectory, it remains in the normal operation mode until it converges to the SEP. In Case B,  $\mathcal{R}(\beta_B) = [-45.20^\circ, 45.20^\circ]$ . Therefore, mode oscillations are expected while  $\delta \in \mathcal{R}(\beta_B) \cap \mathcal{S} = [32.0455^\circ, 45.20^\circ]$ . These mode oscillations are reduced using forced saturation introduced in [4]. The GFM IBR operates as a voltage source from  $t_{b_1} = 0.314$  s, which is shown as point  $b_1$  in Fig. 12(i) and Fig. 13(i). At this point, the GFM IBR enters  $\mathcal{R}(\beta_B) - \mathcal{S}$ .

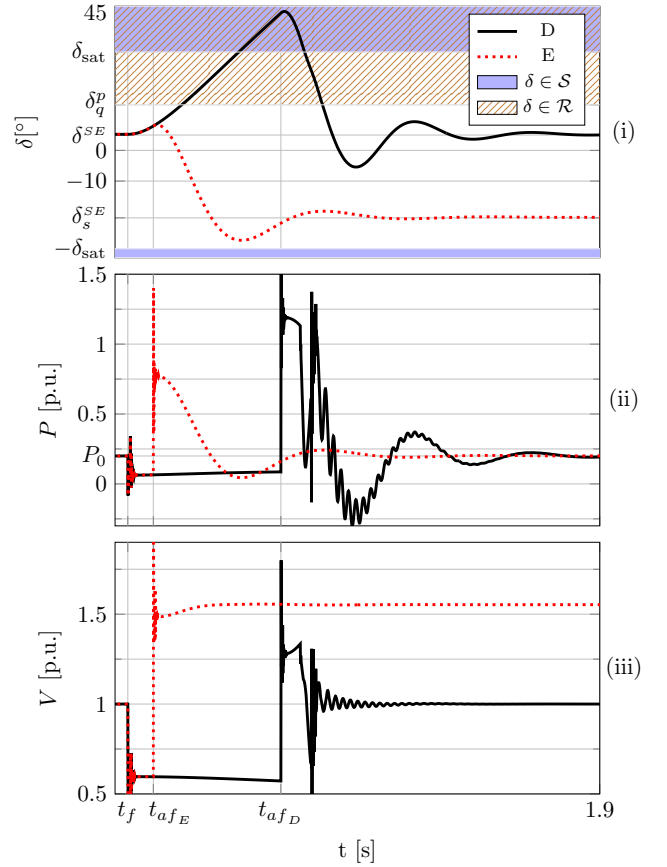


Fig. 14. The GFM IBR's (i) angle, (ii) power, and (iii) voltage in Cases D and E.

Since  $\beta_B < \beta_A < 0$ , more post-fault deceleration is provided in Case B as explained in Section IV. As a result, the angle in Case B converges to the SEP faster than Case A. Therefore,  $\beta$  should be properly selected in practice so that (a) the GFM IBR does not converge to the satSEP, (b) more post-fault deceleration is provided.

The comparison of cases D and E demonstrates that a short fault duration does not necessarily lead to desired consequences. The GFM IBR returns to the normal operation mode with some oscillations and converges to the SEP in Case D as shown in Fig. 14(i). However, in Case E, the post-fault angle is out of both  $\mathcal{R}(\beta_E)$  and  $\mathcal{S}$ . Therefore, it remains in the current-

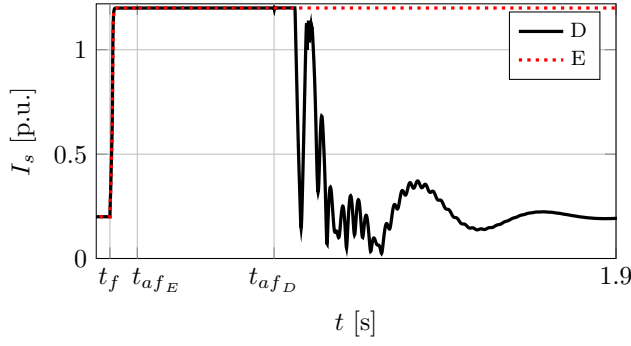


Fig. 15. The GFM IBR's current in Cases D and E.

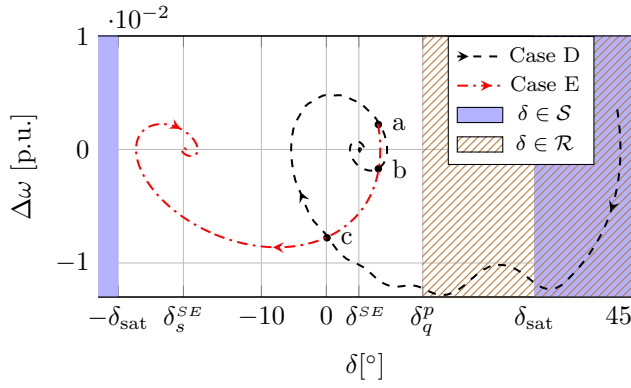


Fig. 16. Post-disturbance trajectories of the GFM IBR in Cases D and E where the solid area and hatched area correspond to the set of entering and returning angles, respectively.

saturation mode as it was during the fault disturbance. Since the power output in the current-saturation mode is more than the power reference at this APC angle, the GFM IBR reduces its angle until it converges to the satSEP, which is out of  $\mathcal{S}$ , as depicted in Fig. 14(i). According to Fig. 14(ii) in both cases the active power output will be the power reference in the steady-state. However, the goal of voltage regulation is not achieved in Case E in contrast to Case D. Fig. 15 also confirms that Case E remains in the current-saturation mode.

Notice that in both Cases C and E, the GFM IBR converges to the satSEP; however, the contributing factors are different. While the satSEP was inside  $\mathcal{S}$  in Case C (condition  $\mathcal{C}_1$  in Section IV), it was out of  $\mathcal{S}$  in Case E. Therefore,  $\mathcal{C}_1$  cannot be the reason for locking into the current-saturation mode. Indeed, the GFM IBR is locked into the current-saturation mode due to condition  $\mathcal{C}_2$ . Therefore, it is concluded that if the GFM IBR is being operated in a light loading, the value of  $\beta$  should be carefully adjusted so that it is not locked into the current-saturation mode after short disturbances.

The dynamic simulations of Cases F and G confirm that the black line in Fig. 17, which is calculated numerically, is the post-fault transient stability border as the black line. This border is much closer to the SEP compared to the border for the unsaturated GFM IBR shown as the brown line in Fig. 17. Fig. 18 shows that the GFM IBR converges to  $(360^\circ + \delta^{SE})$ ,

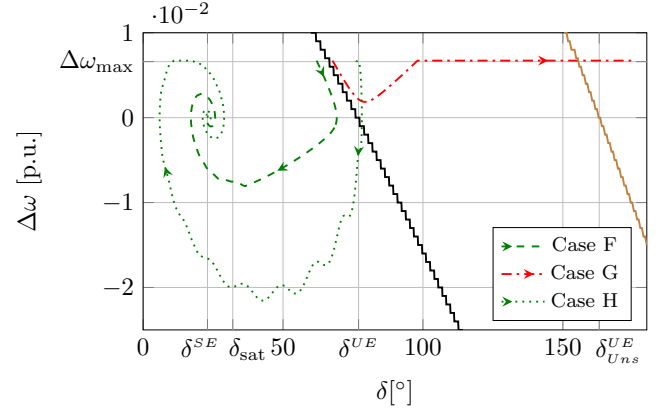


Fig. 17. Post-disturbance trajectories of the GFM IBR in Cases F, G, and H. Black line and brown line are the borders of DOAs for a GFM equipped and not equipped with CRS; respectively.

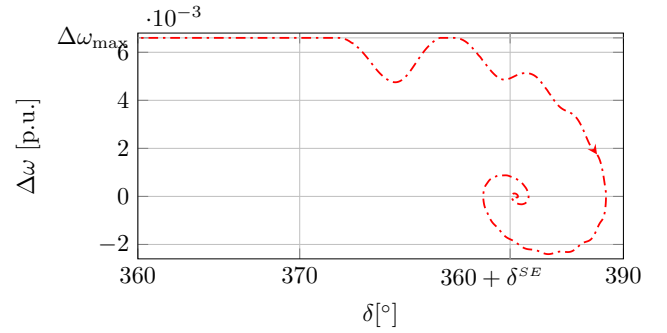


Fig. 18. Trajectory of Case G until convergence to the next SEP after passing the unstable equilibrium point 1.

0) after passing the unstable equilibrium point 1 in Case G. Although, it is theoretically stable, it is not practically desired. The GFM IBR absorbs active power from  $t_{g1} = 0.974$  s until  $t_{g2} = 2.219$  s. It might cause a considerable over-voltage of the DC link capacitor if its capacitance is not big enough, and as a result, the GFM IBR trips. Simulation of Case H reveals that even for a post-fault angle larger than those of Case G, being unsaturated helps transient stability. However, Fig. 20 shows that an overcurrent significantly exceeding the current limit appears and lasts for a considerable length of time duration in Case H. Therefore, Case H is not practical and it is simulated here only to confirm current saturation deteriorates transient stability.

## VII. CONCLUSIONS

The post-disturbance recovery and transient stability analysis for GFM IBRs considering current limitation with constant current angle have been conducted in this paper. These two sets of returning angles and entering angles, which model transition between normal operation mode and current-saturation operation mode have been introduced. The latter only depends on the grid voltage and impedance, and the former depends on the saturated current angle in addition to the grid voltage and impedance and  $X/R$  ratio.

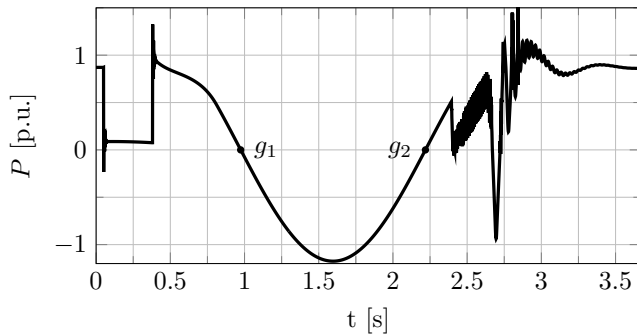


Fig. 19. The GFM IBR's active power injection in Case G.

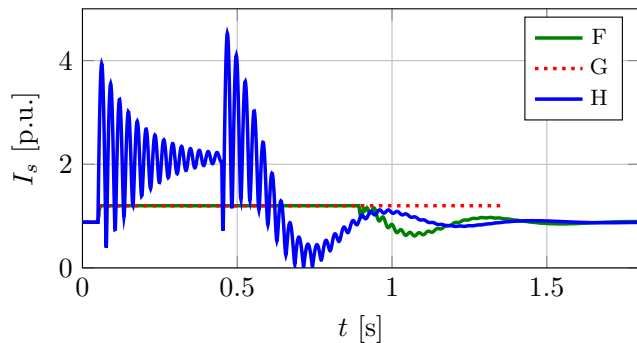


Fig. 20. The current output of the GFM IBR in Cases F, G, and H.

A GFM IBR may not be able to escape from the current saturation and return to the SEP subject to certain static and dynamic conditions; instead, there is a risk of being locked into a stable point in the current-saturation mode (i.e., satSEP) or even loss of synchronism. Even a very short fault disturbance can result in the convergence to the satSEP. The saturated current angle plays a significant role in shaping the post-disturbance dynamics of a GFM IBR. This implies the saturated current angle should be carefully regulated. Besides, the traditional CCT or DOA analyses, which are commonly used for transient stability assessment, should be revisited according to such complex behaviors.

Although the analyses are only tested and verified under fault disturbances in this paper, they can also be extended for other disturbances that cause deviation of the APC angle from its SEP such as terminal voltage phase jump.

#### ACKNOWLEDGMENTS

The authors would like to thank Prof. Yusheng Xue, Prof. Damiano Varagnolo, and Dr. Adria Junyent-Ferre for their invaluable feedback and suggestions.

#### REFERENCES

- [1] K. Zhuang, H. Xin, P. Hu and Z. Wang, "Current Saturation Analysis and Anti-Windup Control Design of Grid-Forming Voltage Source Converter," *IEEE Trans. Energy Convers.*, vol. 37, no. 4, pp. 2790-2802, Dec. 2022, doi: 10.1109/TEC.2022.3208060.
- [2] H. Zhang, W. Xiang, W. Lin and J. Wen, "Grid Forming Converters in Renewable Energy Sources Dominated Power Grid: Control Strategy, Stability, Application, and Challenges," in *Journal of Modern Power Systems and Clean Energy*, vol. 9, no. 6, pp. 1239-1256, November 2021, doi: 10.35833/MPCE.2021.000257.
- [3] M. H. Ravanji, D. B. Rathnayake, M. Z. Mansour and B. Bahrani, "Impact of Voltage-Loop Feedforward Terms on the Stability of Grid-Forming Inverters and Remedial Actions," *IEEE Trans. Energy Convers.*, vol. 38, no. 3, pp. 1554-1565, Sept. 2023, doi: 10.1109/TEC.2023.3246566.
- [4] A. Arjomandi-Nezhad, Y. Guo, B. Pal, and D. Varagnolo, "A Model Predictive Approach for Enhancing Transient Stability of Grid-Forming Converters," *IEEE Trans. Power Syst.*, early access, 2024.
- [5] K.V. kkuni, and Y. Guangya, "Effects of current limit for grid forming converters on transient stability: analysis and solution," *arxiv preprint*, arXiv:2106.13555, June 2021.
- [6] C. Luo, X. Ma, T. Liu, X. Wang, "Controller-Saturation-Based Transient Stability Enhancement for Grid-Forming Inverters," *IEEE Trans. Power Electron.*, vol. 38, no. 2, pp. 2646-2657, 2022.
- [7] Y. Gu, T. C. Green, "Power system stability with a high penetration of inverter-based resources," *Proceedings of the IEEE*, 2022.
- [8] J. Lei, X. Xiang, B. Liu, W. Li, and X. He, "Quantitative and Intuitive VSG Transient Analysis with the Concept of Damping Area Approximation," *IEEE Trans. Smart Grid*, Mar 2023.
- [9] X. Fu, J. Sun, M. Huang, Z. Tian, H. Yan, H. Ho-Ching Iu, P. Hu, and X. Zha. "Large-signal stability of grid-forming and grid-following controls in voltage source converter: A comparative study," *IEEE Trans. Power Electronics*, vol. 36, no. 7 7832-7840, 2020.
- [10] J. Lei, X. Xiang, B. Liu, W. Li, and X. He, "The analysis and calculation of power angle dynamics in grid forming converter under large disturbances based on KBM asymptotic method," *IEEE Trans. Power Electronics*, vol. 38, no. 2, 1494-1508, 2022.
- [11] X. He, L. Huang, I. Subotić, V. Häberle, and F. Dörfler, "Quantitative Stability Conditions for Grid-Forming Converters With Complex Droop Control," *arXiv preprint*, arXiv:2310.09933, 2023.
- [12] T. Liu, X. Wang, F. Liu, K. Xin, and Y. Liu, "Transient stability analysis for grid-forming inverters transitioning from islanded to grid-connected mode," *IEEE Open Journal of Power Electronics*, 3, 419-432, 2022.
- [13] J. Lei, X. Xiang, B. Liu, W. Li, X. He, "Transient Stability Analysis of Grid forming Converters based on Damping Energy Visualization and Geometry Approximation," *IEEE Trans. Ind. Electronics*, 2023.
- [14] N. Rajaei, D. Ramasubramanian, J. Ma, B. Bahrani, "GPST Topic 1: Advanced inverter applications (and requirements) for current-limited grid-forming inverters," 2023.
- [15] B. Fan, T. Liu, F. Zhao, H. Wu and X. Wang, "A Review of Current-Limiting Control of Grid-Forming Inverters Under Symmetrical Disturbances," *IEEE Open Journal of Power Electronics*, vol. 3, pp. 955-969, 2022, doi: 10.1109/OJPEL.2022.3227507.
- [16] S. H. Khan, M. Z. Lazkano, P. Izurza, A. Sanchez-Ruiz, J. C. Aceña and J. Arza, "Synchronization Stability of a Grid Forming Converter Under the Effect of Current Limit in Voltage Dips with VI Based Current Limiting Method: Analysis and Solution," *2022 24th European Conference on Power Electronics and Applications (EPE'22 ECCE Europe)*, Hanover, Germany, pp. P.1-P.9, 2022.
- [17] T. Qoria, F. Gruson, F. Colas, G. Denis, T. Prevost and X. Guillaud, "Critical Clearing Time Determination and Enhancement of Grid-Forming Converters Embedding Virtual Impedance as Current Limitation Algorithm," *IEEE Journal of Emerging and Selected Topics in Power Electronics*, vol. 8, no. 2, pp. 1050-1061, June 2020, doi: 10.1109/JESTPE.2019.2959085.
- [18] X. Xiong, C. Wu and F. Blaabjerg, "Effects of Virtual Resistance on Transient Stability of Virtual Synchronous Generators Under Grid Voltage Sag," *IEEE Transactions on Industrial Electronics*, vol. 69, no. 5, pp. 4754-4764, May 2022, doi: 10.1109/TIE.2021.3082055.
- [19] Y. Zhang, C. Zhang, R. Yang, M. Molinas and X. Cai, "Current-constrained power-angle characterization method for transient stability analysis of grid-forming voltage source converters," *IEEE Trans. Energy Convers.*, vol. 38, no. 2, pp. 1338-1349, Jun. 2023.
- [20] T. Qoria, F. Gruson, F. Colas, X. Kestelyn, and X. Guillaud, "Current limiting algorithms and transient stability analysis of grid-forming VSCs," *Electr. Power Syst. Res.*, vol. 189, p. 106726, 2020.
- [21] B. Fan and X. Wang, "Impact of circular current limiters on transient stability of grid-forming converters," *Proc. IEEE Int. Power Electron. Conf. (IPEC-Himeji Asia)*, pp. 429-434, 2022.
- [22] L. Huang, H. Xin, Z. Wang, L. Zhang, K. Wu, J. Hu, "Transient stability analysis and control design of droop-controlled voltage source converters

- considering current limitation,” *IEEE Transactions on Smart Grid*, vol. 10 no. 1, 578-591, 2017.
- [23] X. Lyu, W. Du, S. M. Mohiuddin, S. P. Nandanoori, M. Elizondo, “Improved Transient Stability Analysis of Multi-Loop Droop-Controlled Grid Forming Inverters with Current Limiter,” *In 2024 IEEE Power & Energy Society Innovative Smart Grid Technologies Conference (ISGT)* (pp. 1-5). IEEE, Feb. 2024.
- [24] A. Quedan, W. Wang, D. Ramasubramanian, E. Farantatos, S. Asgarpour, “Dynamic behavior of combined 100 % IBR transmission and distribution networks with grid-forming and grid-following inverters,” *In 2023 IEEE Power & Energy Society Innovative Smart Grid Technologies Conference (ISGT)* (pp. 1-5). IEEE, Jan. 2023.
- [25] T. Qoria, E. Rokrok, A. Bruyere, B. François, X. Guillaud, “A PLL-free grid-forming control with decoupled functionalities for high-power transmission system applications,” *IEEE Access*, 8, 197363-197378, 2020.
- [26] G. Wang, L. Fu, Q. Hu, C. Liu and Y. Ma, “Transient Synchronization Stability of Grid-Forming Converter During Grid Fault Considering Transient Switched Operation Mode,” *IEEE Trans. Sust. Energy*, vol. 14, no. 3, pp. 1504-1515, July 2023, doi: 10.1109/TSTE.2023.3236950.
- [27] S.P. Me, M.H. Ravanji , B. Leonardi, D. Ramasubramanian, J. Ma, S. Zabihi, and B. Bahrani, “Transient Stability Analysis of Virtual Synchronous Generator Equipped with Quadrature-Prioritized Current Limiter,” *IEEE Trans. Power Electronics*, May 2023.
- [28] Y. Lu, Y. Li, T. Mu, C. Shao, J. Liu, D. Yang, Z. Du, “Segmental equal area criterion for grid forming converter with current saturation,” *International Journal of Electrical Power & Energy Systems*, 159, 110015, 2024.
- [29] Y. Li, Y. Lu, J. Yang, X. Yuan, R. Yang, S. Yang, H. Ye, and Z. Du, “Transient stability of power synchronization loop based grid forming converter,” *IEEE Trans. Energy Convers.*, 2023.
- [30] E. Rokrok, T. Qoria, A. Bruyere, B. Francois, and X. Guillaud, “Transient stability assessment and enhancement of grid-forming converters embedding current reference saturation as current limiting strategy,” *IEEE Trans. Power Syst.*, vol. 37, no. 2, pp. 1519–1531, Mar 2022.
- [31] B. Fan and X. Wang, “Fault Recovery Analysis of Grid-Forming Inverters With Priority-Based Current Limiters,” *IEEE Trans. Power Syst.*, doi:10.1109/TPWRS.2022.3221209, 2022.
- [32] A. Yazdani, R. Iravani, “Voltage-sourced converters in power systems: modeling, control, and applications,” *John Wiley and Sons*, 2010.
- [33] P. Kundur, *Power System Stability and Control*, New York, NY, USA: McGraw-Hill, 1994.
- [34] L. Huang, H. Xin, Z. Wang, K. Wu, H. Wang, J. Hu, C. Lu, “A virtual synchronous control for voltage-source converters utilizing dynamics of DC-link capacitor to realize self-synchronization,” *IEEE Journal of Emerging and Selected Topics in Power Electronics*, 5(4), pp.1565-1577, 2017.
- [35] MathWorks. (2021). MATLAB Simulink R2021b [Software]. Natick, MA: The MathWorks, Inc.
- [36] A. Tayyebi, D. Groß, A. Anta, F. Kupzog and F. Dörfler, “Frequency Stability of Synchronous Machines and Grid-Forming Power Converters,” *in IEEE Journal of Emerging and Selected Topics in Power Electronics*, vol. 8, no. 2, pp. 1004-1018, June 2020, doi: 10.1109/JESTPE.2020.2966524.